ADVANCED ENERGY MATERIALS
www.advenergymat.de

High-Efficiency and Durable Inverted Perovskite Solar Cells with Thermally-Induced Phase-Change Electron Extraction Layer

Xin Li, Yun Meng, Ruizhe Liu, Zhiyao Yang, Yan Zeng, Yuanping Yi, Wei E. I. Sha,* Yi Long,* and Junyou Yang**

Reducing carrier recombination and facilitating charge extraction at the interface is of great significance to improve the device performance of perovskite solar cells (PSCs) towards commercial use. However, there has been little work done concerning transportation and recombination mechanism at the interface of the metal electrode and the electron transport layer in inverted PSCs. Herein, a new strategy of interface modification is reported that leverages the unique metal-to-insulator transition (MIT) characteristics of vanadium dioxide which is inserted as the electron extraction layer (EEL) in p-i-n planar PSCs. Benefiting from the suitable intermediate energy level of VO_2, the optimized device shows a power conversion efficiency (PCE) up to 22.11% with negligible hysteresis, as compared to the 20.96% benchmark at room temperature. Interestingly, the PCE of VO_2-based PSC increases to over 23% at 85 °C, which can be attributed to the dramatic change in the electrical properties and better electron extraction caused by the MIT of VO_2 beyond its critical phase-change temperature. In addition, the encapsulated VO_2-PSC shows superior thermal stability for 1000 h at 85 °C under 1 Sun illumination, maintaining over 90% of initial PCE. This work initiates the state-of-art concept of inserting thermally-induced phase-transition material as an EEL to achieve efficient and durable perovskite photovoltaics.

1. Introduction

Perovskite solar cells (PSCs) have been extensively attracted attention owing to the superior optoelectronic properties of perovskite absorber materials (e.g., high absorption coefficient, tunable direct bandgap, long carrier diffusion length, and low-temperature solution fabrication).[1–8] To date, the power conversion efficiency (PCE) of regular "n-i-p" PSC has been increased from 3.8% to a certified value of 25.6%,[9,10] making it comparable with other thin-film photovoltaic technologies. However, inverted "p-i-n" PSC has become the cutting-edge research in the field of perovskite photovoltaics because it has shown great potential for further studies of flexible photovoltaics, perovskite/Si or perovskite/CIGS, and all-perovskite tandem solar cells.[11–14] So far, significant efforts have been dedicated to the further improvements of inverted PSCs' efficiency, with an aim to increase its competitiveness among regular structure PSCs. In addition, the long-term

X. Li, J. Yang
State Key Laboratory of Material Processing and Die & Mould Technology
School of Materials Science and Engineering
Huazhong University of Science and Technology
Wuhan 430074, P. R. China
E-mail: xin.li@nus.edu.sg; jyyang@hust.edu.cn

X. Li
Solar Energy Research Institute of Singapore
National University of Singapore
Singapore 117574, Singapore

Y. Meng, Y. Long
School of Materials Science and Engineering
Nanyang Technological University
Singapore 639798, Singapore
E-mail: longyi@ntu.edu.sg

R. Liu, Z. Yang, W. E. I. Sha
State Key Laboratory of Modern Optical Instrumentation
College of Information Science and Electronic Engineering
Zhejiang University
Hangzhou 310027, P. R. China
E-mail: weisha@zju.edu.cn

Y. Zeng, Y. Yi
Beijing National Laboratory for Molecular Sciences
CAS Key Laboratory of Organic Solids
Beijing 100190, P. R. China

Y. Long
Singapore-HUJ Alliance for Research and Enterprise (SHARE)
Campus for Research Excellence and Technological Enterprise (CREATE)
Singapore 138602, Singapore

Y. Long
Sino-Singapore International Joint Research Institute (SSIJRI)
Guangzhou 510000, P. R. China

The ORCID identification number(s) for the author(s) of this article can be found under https://doi-org.libproxy1.nus.edu.sg/10.1002/aenm.202102844.

DOI: 10.1002/aenm.202102844

operational stability of PSCs still remains the key issue towards commercialization.

Hole transport layers (HTLs) play a vital role in delivering PSCs superior in both their performance and stability, and the applied HTLs in this inverted structure have been well studied. For instance, researchers have found that replacing the acidic and hygroscopic PEDOT: PSS with alternative materials, like PTAA,[15] poly-TPD,[16] or several self-assembled monolayers (SAMs),[13,14] can prominently improve the device performance. Furthermore, several low-cost inorganic p-type HTLs, such as NiO_x,[17] CuO_x,[18] $CuCrO_2$,[19] $CuGaO_2$,[20] CuSCN,[21] and CuI,[22] have also been widely employed in both regular and inverted PSCs, with an attempt to enhance device stability. However, the back-contact electron transport layers (ETLs) stay an under-researched topic for inverted PSCs. So far, fullerene derivatives are commonly used for ETLs in inverted PSCs.[23] The PSCs based on PCBM (or C_{60}) tend to exhibit severe hysteresis behavior because difference between the Fermi level of PCBM (or C_{60}) and the work function of the metal electrodes (Ag, Cu, Al) lead to the formation of a Schottky barrier at the interface, which causes charge carrier accumulation at the interface, thus weakening the device performance.[24–26] BCP has been used to tackle this issue,[27–29] as they can provide better-matched energy level between PCBM (or C_{60}) and metal electrodes to form ohmic contact. Unfortunately, such BCP is not stable for long-term device operations.[28] In addition, SnO_x (or other metal oxides) was also employed as ETLs in inverted PSCs. However, the C_{60} interface layer has been inserted between the perovskite and SnO_x in inverted PSCs to prevent ALD or sputtering damages on the perovskite films.[29,30] However, most of these researches mainly focus on the carrier transportation and charge recombination between ETLs and perovskite films. Little work has been studied systematically on charge recombination and extraction at the interface between ETLs and metal electrode in inverted PSCs. More importantly, it is also related to the high efficiency and long-term stability inverted PSCs towards the commercialization.

Herein, we report a new strategy of interface modification that leverages the unique metal-to-insulator transition (MIT) characteristic of vanadium dioxide (VO_2) that is inserted as the inorganic top electron extraction layer (EEL) in p-i-n planar PSCs. Due to the better cascade band alignment between ETL and metal electrode, a significantly enhanced photovoltaic performance, together with hysteresis-free behavior, has achieved in the PSCs with such VO_2 layer. The champion device with VO_2 presents a high PCE of 22.11%, compared with 20.96% of the control device at room temperature. Interestingly, the highest efficiency of optimized VO_2-PSC can be increased to over 23% at 85 °C due to the dramatic change in the electrical properties by phase transition process under elevated temperature—the electron mobility of the "metallic" state of VO_2 at 85 °C becomes nearly 100 times larger than the "insulator" state of VO_2 at room temperature. The enhanced charge transportation and reduced interface recombination for VO_2-based PSC lead to improvement of device performance even at high temperature. Encouraging results show that device based on VO_2 presents better operational stability under different stress conditions, such as different levels of air humidity, light illumination, and temperature elevation. In particular, the device with VO_2 shows superior thermal stability, maintaining over 85% initial efficiency after 500 h at 85 °C heat without any encapsulation. More importantly, the encapsulated VO_2-PSC can retain over 90% of its initial PCE under 1 Sun illumination at 85 °C. Overall, our results have identified VO_2 phase-change material as a potential candidate n-type electron extraction layer candidate for future commercial applications.

2. Results and Discussion

As a versatile transition, metal oxide semiconductor, monoclinic (M), and rutile (R) phase VO_2 have aroused great attention due to the MIT at a critical temperature of about 68 °C.[31] **Figure 1**a presents the typical reversible phase transition process of VO_2 between a low-temperature monoclinic (M) phase and a high-temperature rutile (R) phase.

The X-ray diffraction (XRD) pattern of the as-prepared VO_2 nanoparticles is shown in Figure S1, Supporting Information. The main diffraction peaks assigned to the (011), (−211), (−212), (220), (022), and (031) peaks at 27.9°, 36.8°, 42.2°, 55.5°, 57.6°, and 64.9°, respectively, are well-indexed as the VO_2 compound with a monoclinic structure (JCPDS card no. 043-1051). It can be seen from the differential scanning calorimetry (DSC) results in Figure S2, Supporting Information, the DSC curves of the VO_2 nanoparticles have displayed endothermic peak at 67.2 °C and exothermic peak at 59.3 °C, indicating a typical MIT characteristic of VO_2 (M). Figure 1b shows the transmission electron microscopy (TEM) image of some particles scraped from the as-coated VO_2 film on the quartz glass. The high-resolution lattice fringes shown in Figure 1c with interplanar spacing of 0.32 nm are consistent with the (111) crystal plane of the VO_2 (M). Generally, a series of vanadium oxides with their respective oxidation states during various synthesis methods and annealing processes, such as VO (V^{2+}), V_2O_3 (V^{3+}), VO_2 (V^{4+}), and V_2O_5 (V^{5+}), are prone to be formed.[32] In order to further precisely confirm the surface composition and chemical element valence state of the VO_2 film, a high-resolution X-ray photoelectron spectroscopy spectrum for O 1s and V 2p core levels is demonstrated in Figure S3, Supporting Information. Two peaks, located at 516.42 and 524.06 eV, are associated with the spin-orbit splitting of V $2p_{3/2}$ and $V2p_{1/2}$, which are in good agreement with the V^{4+} oxidation state.[33] In addition, the peak at 529.96 eV is assigned to O 1s owing to the binding energy of V-O.

Furthermore, the phase transition for VO_2 (M/R) is confirmed as the crystal face variation exhibited by temperature-dependent XRD patterns, shown in Figure S4, Supporting Information, and Figure 1d. It can be indicated that the peak at 27.9° identified as (011) VO_2 (M) shifts gradually to the 27.6° as (110) VO_2 (R) under an increasing temperature from 30 °C to 100 °C. In addition, the in situ Raman spectra shown in Figure 1e can also indicate the reversible phase transition feature of VO_2 film. At the temperature of 30 °C, Raman peaks of 194, 224, 310, 389, 498, 615 cm^{-1} could all be attributed to VO_2 (M), which is consistent with other literature.[34] However, there are no peaks in Raman spectra of the VO_2 film at 90 °C, except for the substrate peak. It manifests a gradual transformation of VO_2 (M) to VO_2 (R) with the gradual disappearance of all

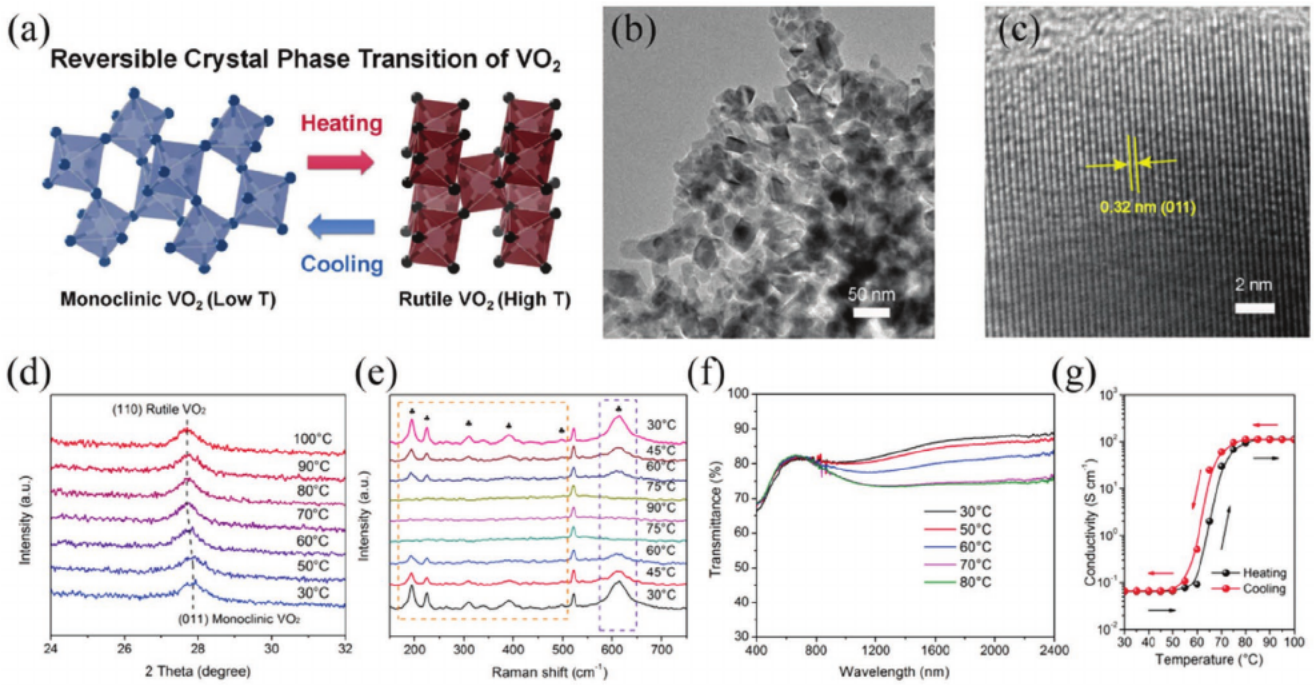

Figure 1. a) Illustration of the reversible crystal phase transition of VO_2 between the low-temperature monoclinic (M) phase and the high-temperature rutile (R) phase. b) TEM image, and c) HRTEM image of the VO_2 film. d) Magnified (110) plane in the XRD patterns of VO_2 film. e) In situ Raman spectra of VO_2 film based on the fully-reversible phase transition under heating and cooling. f) Transmittance spectra of VO_2 film at different temperature. g) Temperature-dependent conductivity based on the fully reversible phase transition.

characteristic peaks when temperature was increased from 30 to 90 °C during heating process. In contrast, the as-mentioned peaks appear again from 90 to 30 °C during cooling process. It is well known that VO_2 (M) indicates a distorted structure with zigzag-type V—V atomic chains at room temperature and it slowly changes to VO_2 (R) with straight V—V chains above its critical temperature of 68 °C, accompanied with significant physical property changes, such as the optical and electrical properties.[35] For instance, regarding the optical property of VO_2 film, transmittance spectra (Figure 1f) and absorbance spectra (Figure S5, Supporting Information) all present that there is no difference in the visible region from 300 to 900 nm, but a dramatic change in the near-infrared range above 900 nm. As for the electrical property shown in Figure 1g, the conductivity of VO_2 (R) at relatively high temperature is approximately 1000 times larger than that of VO_2 (M) at room temperature. It can be clearly seen that the "insulator phase" of VO_2 (M) at room temperature showed the conductivity of $\approx 6.5 \times 10^{-2}$ S cm^{-1}, while "metallic phase" of VO_2 (R) at high temperature indicated higher conductivity of 1.12×10^{2} S cm^{-1}. Even under room temperature, the conductivity for "insulator phase" of VO_2 showed high conductivity compared with SnO_2 or TiO_2 as measured in our previous work.[6,22] That is to say the "insulator phase" of VO_2 is not insulating at room temperature.

The photographs of the perovskite film and perovskite covered by VO_2 layer are illustrated in Figure S6, Supporting Information. It is obviously seen that there are quite different colors between the perovskite film and VO_2 film. The scanning electron microscopy (SEM) images of the as-deposited perovskite film and the perovskite directly covered by VO_2 film are shown in Figure S7, Supporting Information. It can be observed that a smooth, large-grain, and pinhole-free perovskite film has been formed in Figure S7a,b, Supporting Information. More importantly, the morphology of VO_2 shown in Figure S7c,d, Supporting Information, is different from that of perovskite, indicating that the VO_2 film can compactly cover the perovskite layer. These SEM results also confirm that the spin-coated VO_2 film is compatible with the organic-inorganic hybrid perovskite layer. The energy-dispersive X-ray spectrometer mappings of V and O elements shown in Figure S8, Supporting Information, confirm that the VO_2 layer has a homogeneous composition distribution. In addition, Cs, Pb, I, and Br elements for the perovskite film can also be detected.

To verify the effect of VO_2 layer on photovoltaic performance, the inverted planar PSC with the device architecture of ITO/PTAA/perovskite/PCBM/BCP (5 nm)/VO_2/Ag was shown in **Figure 2**a. As seen in Figure S9a,b, Supporting Information, VO_2 film shows high transmittance in the visible-light wavelength and the calculated optical bandgap of VO_2 film is approximately 3.21 eV, which is also consistent with the previous experimental results.[36,37] As displayed in Figure S9c,d, Supporting Information, the conduction band minimum (CBM) of VO_2 can be confirmed by ultraviolet photoelectron spectroscopy spectra. As seen from the corresponding energy level diagram depicted in Figure 2b, the VO_2 has a considerably well-matched energy alignment with the perovskite layer, resulting in better device performance. The dependence of the champion device performance on the thickness of VO_2 layer was also investigated to identify the optimal thickness for PSCs shown in Figure S10, Supporting Information, and the corresponding photovoltaic

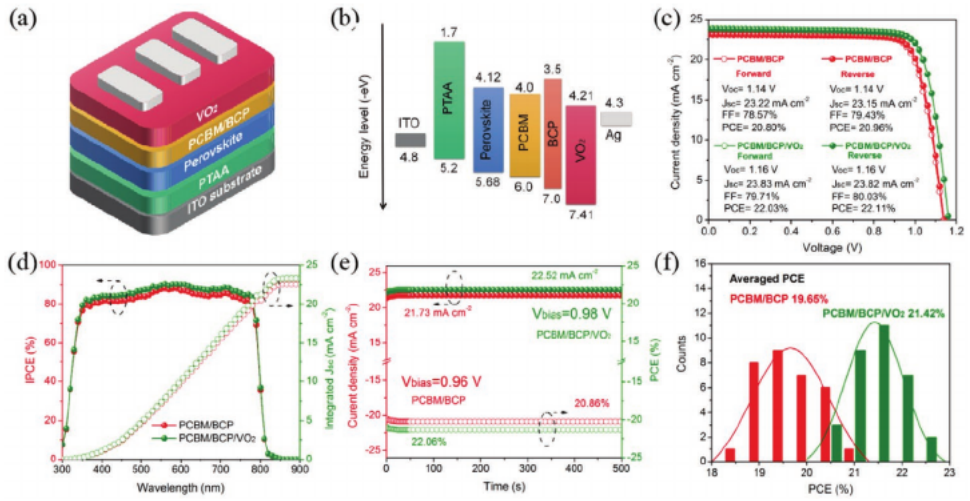

Figure 2. a) Schematic illustration of a typical inverted PSC based on VO_2 layer. b) Corresponding energy band diagram of an inverted device structure. c) *J–V* curves of the PSCs based on PCBM/BCP (5 nm) and PCBM/BCP (5 nm)/VO_2 ETLs measured under different scan directions. d) IPCE spectra of the champion PSCs with and without VO_2 layer. e) Stabilized power output of the devices with and without VO_2 layer tracked at the maximum power point (MPP) under 1 Sun AM 1.5G illumination. f) Histograms of PCEs for 32 cells based on PCBM/BCP (5 nm) and PCBM/BCP (5 nm)/VO_2, respectively.

parameters are summarized in Table S1, Supporting Information. The sufficient thickness of VO_2 film is necessary for achieving efficient electron transporting and hole blocking. However, the devices based on thicker VO_2 layers (for example, larger than 30 nm), especially for the 90 nm VO_2, showed inferior performance with relatively low V_{oc} and FF, and particularly worse J_{sc} owing to the high series resistance. This result is further ascertained by the statistical PCE as a function of thickness shown in Figure S11, Supporting Information. Thus, the optimal thickness for the VO_2 layer was suggested to be around 30 nm in this work and a corresponding cross-sectional SEM image of an optimal device is presented in Figure S12, Supporting Information.

The *J–V* curves of the optimized devices with and without VO_2 are exhibited in Figure 2c. As the control device, the PSC without VO_2 shows a relatively low PCE of 20.96% with V_{oc} of 1.14 V, J_{sc} of 23.15 mA cm^{-2}, and FF of 79.43% under standard AM1.5 solar illumination. It was found that the device based on 30 nm VO_2 layer demonstrates remarkable PCE of 22.11% with V_{oc} of 1.16 V, J_{sc} of 23.82 mA cm^{-2}, and FF of 80.03%, revealing that higher V_{oc}, higher FF, and the particularly higher J_{sc} contributed to the enhanced device. Both devices with and without VO_2 show negligible hysteresis behavior, which is common in inverted structure PSCs and consistent with the previous reports. To verify the precision of the J_{sc} values from the *J–V* curves and evaluate the photocurrent enhancement, the incident photon-to-electron conversion efficiency (IPCE) spectra of both devices are demonstrated in Figure 2d. The integrated current densities calculated from the IPCE curves are 22.53 and 23.29 mA cm^{-2} for the devices without and with VO_2 layer, respectively, which are in excellent agreement with the J_{sc} values obtained from the *J–V* curves within the margin of error. In addition, the stabilized current densities measured at constant biases of 0.96 and 0.98 V near the maximum power point for the devices without and with VO_2 layer are shown in Figure 2e, revealing steady-state PCEs of 20.86% and 22.06%, respectively. Furthermore, a statistical comparison of the averaged PCEs of 32 separate cells without and with VO_2 layer are presented in Figure 2f. As calculated, the averaged PCEs for devices without and with VO_2 are 19.65% and 21.42%, respectively.

As an efficient electron extraction layer, superior electron extracting and efficient hole blocking ability that can facilitate charge flowing from ETLs to perovskite and reduce the recombination at the interface of ETLs/metal electrode and excellent electrical properties to transport carrier with minimized dissipation loss inside the ETLs are both required for high-performance inverted PSC.[38,39] To investigate the interfacial charge carrier dynamics between perovskite and different ETLs, steady-state photoluminescence (PL) and time-resolved PL (TRPL) spectra were obtained accordingly for the perovskite films coated with VO_2, PCBM, PCBM/VO_2 layers, respectively. As can be seen in **Figure 3**a, the bare perovskite film indicated the strongest PL intensity due to the efficient radiative recombination of the photogenerated carriers, while it was apparently quenched upon contacting with different ETLs.[40,41] The perovskite covered by VO_2 showed substantially quenched PL, suggesting efficient charge extraction from perovskite to VO_2. However, the perovskite-coated PCBM demonstrated more quenched PL compared with that coated inorganic VO_2, indicating better contact between perovskite and PCBM. In addition, the perovskite/PCBM/VO_2 exhibited a slightly faster quenched PL than the perovskite/PCBM film, which might be ascribed to the cascade energy alignment in perovskite/PCBM/VO_2 shown in Figure 2b. The conclusion obtained from PL spectra is further verified by the TRPL spectra, as shown in Figure 3b and all parameters are listed in Table S2, Supporting Information. Compared to the perovskite itself (τ = 157.6 ns), perovskite coated by VO_2, PCBM, PCBM/VO_2 exhibits further reduced lifetime of τ = 46.4, 32.9, and 25.4 ns, respectively. Obviously, the perovskite/PCBM/VO_2 film manifested the much shorter biexponential decay than any other perovskite/ETL film, providing a proof of the superior electron-extraction ability of the

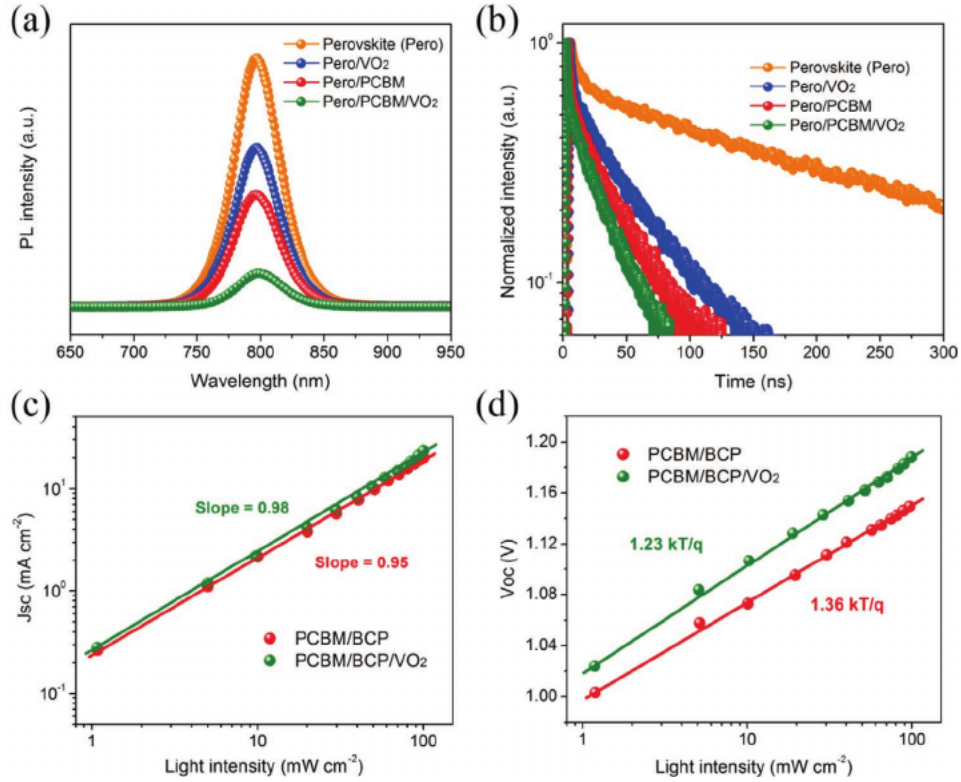

Figure 3. a) Steady-state PL spectra and b) time-resolved PL spectra of perovskite only and perovskite coated with different ETLs, respectively. Light-intensity dependent c) J_{sc} and d) V_{oc} for the devices with and without VO_2 layer, respectively.

PCBM covered by VO_2 layer. Besides, electrochemical impedance spectroscopy (EIS) was also obtained to investigate the charge transport within the PSCs. The charge recombination resistance (R_{rec}) extracted from the low-frequency component of Nyquist plots shown in Figure S13, Supporting Information, suggests higher resistances for the VO_2-based devices as compared to the control one.[42] This result is in good accordance with the PL and TRPL spectra.

To further understand the dynamic recombination and charge carrier lifetimes of the devices without and with VO_2 layer, transient photocurrent (TPC) and transient photovoltage (TPV) were obtained and the results are shown in Figure S14, Supporting Information.[43,44] The device with VO_2 revealed a faster photocurrent decay than the device without VO_2 layer shown in Figure S14a, Supporting Information, suggesting a more efficient charge carrier extraction at the perovskite/ETL interface. Moreover, the longer photovoltage decay in the device with VO_2 layer than that in device without VO_2 implied that the charge carriers possess a longer time to achieve the spatial separation of the photogenerated electron/hole pair in the device (Figure S14b, Supporting Information), which could suppress the non-radiative charge recombination and thus improve device performance.[45–47]

Furthermore, both devices were also characterized by light intensity-dependent photocurrent density and photovoltage. As shown in Figure 3c, the device with VO_2 layer showed a slope closer to 1 for the plot of J_{sc} as a function of light intensity, revealing reduced non-radiative recombination within the device, which is consistent with the result obtained from TPV decay curve.

In addition, the light intensity dependence of the V_{oc} is shown in Figure 3d. The device with VO_2 layer delivers a slightly lower slope of 1.23 kT/q than that of the device without VO_2 (a slope of 1.36 kT/q), where K is the Boltzmann constant, T is the absolute temperature, and q is the elementary charge. This indicates that the trap-assisted Shockley–Read–Hall recombination has been further suppressed for the device based on VO_2 layer.[48] Moreover, the space charge limited current analysis based on electron-only devices was carried out to estimate the electron trap density (N_t) and trap-assisted recombination in devices with and without VO_2 layer shown in Figure S15, Supporting Information. The trap-filled limit voltage (V_{TEL}) determined as the onset voltage TFL region can be utilized to calculate N_t with the equation ($N_t = 2\varepsilon_0\varepsilon_r V_{TEL}/qL^2$, where ε_0 is the vacuum permittivity, ε_r is the relative dielectric constant, and L is the thickness of the perovskite film).[49,50] The lower V_{TEL} value of 0.175 V and correspondingly lower N_t of 1.03×10^{16} cm^{-3} for the device with VO_2 layer were obtained, compared to the values obtained for device without VO_2 ($V_{TEL} = 0.303$ V, $N_t = 1.78 \times 10^{16}$ cm^{-3}). More importantly, it was also notably proved that less trap-recombination center appears non-radiative recombination is greatly suppressed for the VO_2 based PSC.

To further investigate the properties of the interface, the capacitance (C)-voltage (V) characteristics of the devices without and with VO_2 were measured in the dark, as presented in Figure S16, Supporting Information. The built-in potential (V_{bi}) obtained from the $1/C^2$-V Mott–Schottky plots for the PCBM/VO_2 based device (1.12 V) is slightly higher than the PCBM one (1.08 V), which directly confirms that the device with VO_2 layer

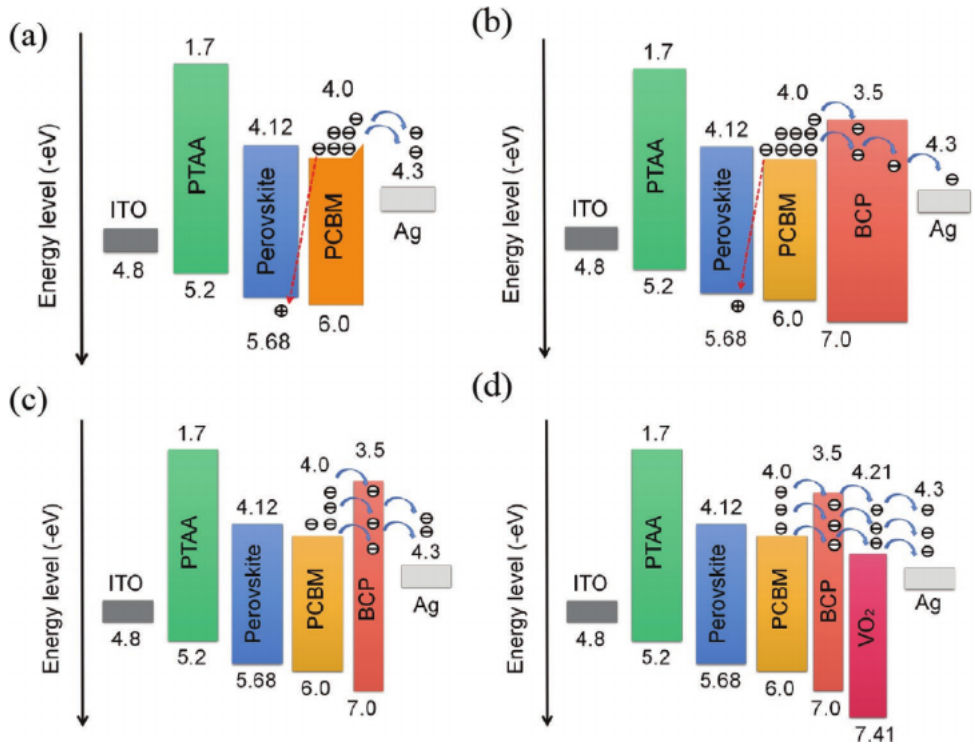

Figure 4. The energy diagram and charge transport mechanism of PSCs with various ETLs. a) Device without BCP layer. b) Device with thick BCP layer. c) Device with 5 nm thin BCP layer in this work. d) Device with 5 nm BCP and VO_2 layer.

shows fast charge transfer and reduced charge accumulation at the interface between perovskite and cathode.

As mentioned above, all the results indicated the VO_2 layer could accelerate the carrier transportation and suppress the non-radiative recombination at the interface. The enhanced charge transportation can be confirmed by PL, TRPL, EIS, TPC as well as light intensity dependence of J_{sc}. The non-radiative recombination is related to the defect density of bulk perovskite, and also to the charge collection at all interfaces in the device, such as better band alignments for transporting majority carriers and blocking minority carriers.[51] That is to say, it is not just attributed to the interface, which is directly in contact with the perovskite layer. Few works discussed the interface between PCBM/BCP and electrode, which is exactly the novelty of this work. The measurement of TPV and light intensity dependence of V_{oc} data can directly indicate the reduced non-radiative recombination of the device based on the VO_2 layer. The corresponding energy diagram and physical charge transport mechanism of PSCs with various ETLs can be explained in **Figure 4**.

The impact of BCP on the carrier transportation of PSCs has been clarified in some previous reports.[52,53] The device without the BCP layer, charge accumulation would occur at the interface between the PCBM and Ag due to the existence of Schottky barrier (though not high), leading to inferior device performance, shown in Figure 4a.[54–56] The bulk thick BCP layer shown in Figure 4b will induce the extraction barrier for the majority carriers (electrons) leading to the electron accumulation at the PCBM/BCP interface. The charge accumulation will greatly increase the non-radiative recombination at the PCBM/BCP interface.[52] However, when the thickness of the BCP layer is reduced to be 5 nm in this work and the BCP cannot be regarded as the bulk material. Meanwhile, 5 nm is thin enough for electron tunneling. Therefore, charge accumulation occurs at the PCBM/BCP/Ag interfaces is insignificant, which implies good ohmic contact has been established in-between these layers, shown in Figure 4c. Tunneling of electrons and pinning the Fermi level will occur at the PCBM/BCP/Ag interfaces, which equivalently lower the extraction barrier formed at the PCBM/BCP interface, that is, electron affinity of BCP is equivalently lowered, as confirmed by the previous work.[57] Consequently, the electron transportation will be improved significantly. When VO_2 is inserted between the Ag and BCP layers, better ohmic contact is expected shown in Figure 4d, Due to the facilitated electron transportation from the PCBM/BCP layer to electrode via the VO_2 layer, the electron accumulation at the PCBM/BCP/Ag interface will be further reduced, which also reduce the non-radiative recombination.

To further highlight the feature of VO_2 layer used in PSCs as thermally-induced phase material mentioned above, the *J*–*V* curves of the devices without and with VO_2 layer were measured at 25 and 85 °C in N_2 atmosphere, respectively. As is known, the phase transition temperature of VO_2 point is nearly 70 °C shown in Figure 1 and the perovskite-based devices normally will be measured at 85 °C for thermal stability, thus in this work, PSCs were measured both at room temperature (25 °C) and high temperature (85 °C) to check whether the phase-changed VO_2 would affect the device performance as we expected. We first measured the initial efficiency of devices at 25 °C, then we increased temperature to 85 °C in 10 °C or 20 °C steps; when the temperature arrived at 85 °C, we waited

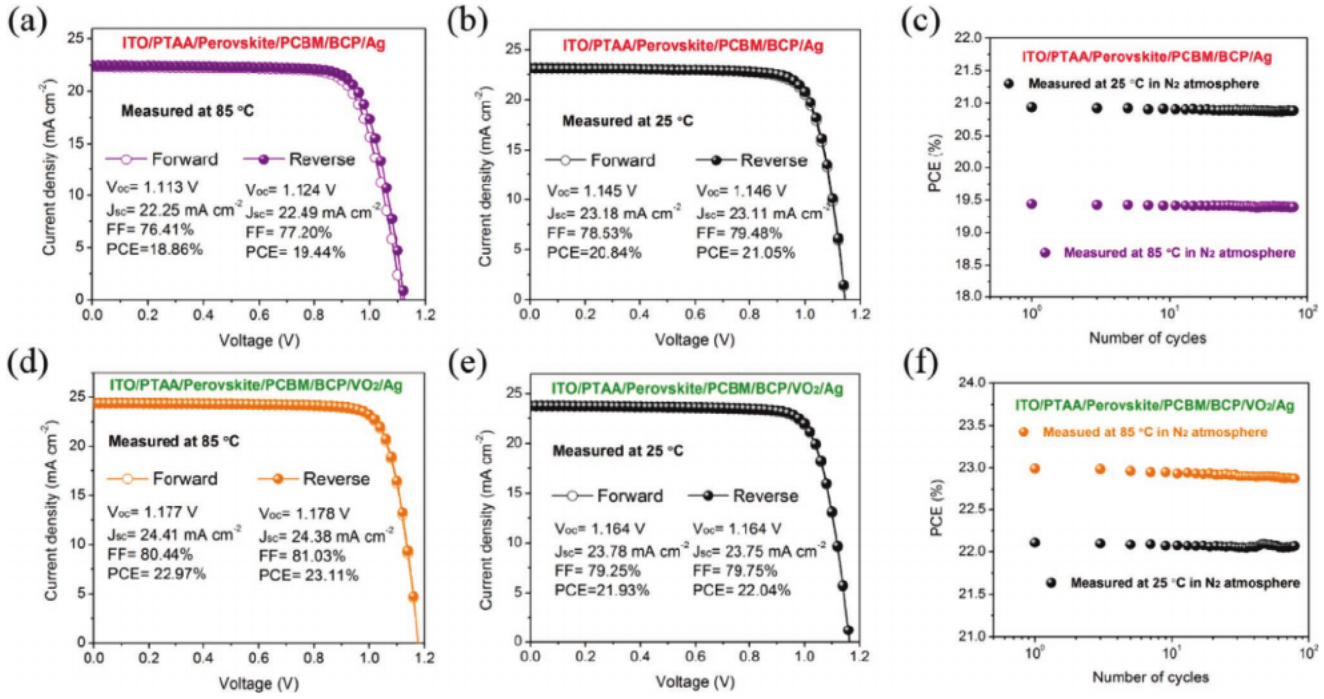

Figure 5. a) *J–V* curves of the control device measured at 85 °C. b) *J–V* curves of the control device measured at 25 °C after the device cooling down from 85 to 25 °C room temperature. c) Cycle stability of control device between 25 and 85 °C. d) *J–V* curves of the VO_2-based device measured at 85 °C. e) *J–V* curves of the VO_2-based device measured at 25 °C after the device cooling down from 85 to 25 °C room temperature. f) Cycle stability of control device between 25 and 85 °C.

≈10 min for the MPP to stabilize, and then finally back at room temperature, and measured it again. As shown in **Figure 5**a, the optimal control device showed the PCE of 19.44% measured at 85 °C with V_{oc} of 1.124 V, J_{sc} of 22.49 mA cm^{-2}, and FF of 77.20%. Then, the control device was measured after the device cooling down from 85 to 25 °C room temperature (Figure 5b). Although the PCE of control device measured at 85 °C is lower than that measured at 25 °C, especially for V_{oc} and FF, resulting in the increased intrinsic carrier concentration of the active perovskite semiconductor at elevated temperature which in turn will increase the dark saturation current and thus reduce the V_{oc} and also will affect the FF,[58] the PCE will return to normal when measured again at room temperature (Figure 5c), which is consistent with Detailed-Balance Principle in Solar Cell Physics,[59] suggesting a good cycle stability shown in Figure 5c. From Figure 5a–c, the temperature coefficient of control device is around –0.12 rel% °C^{-1}, which is exactly in accordance with the literature.[58] The good cycle stability of the control device from heating to cooling and low temperature coefficient of control device could help exclude the effect of perovskite degradation process. To our surprise, the optimal device based on VO_2 layer shows a high PCE over 23% at 85 °C, with V_{oc} of 1.177 V, J_{sc} of 24.38 mA cm^{-2}, and FF of 81.03% (Figure 5d), which is among the highest efficiency inverted PSCs summarized in Table S3, Supporting Information. In addition, the PCE of VO_2-based PSC at 85 °C is higher than that of device with VO_2 layer at 25 °C, which is contrary to the results of the control device (Figure 5e). It is also indicated that the VO_2-based PSC shows superior thermal cycle stability from 85 to 25 °C (Figure 5f). Moreover, we also measured the VO_2-based PSC at 45 and 65 °C (below the phase-changed temperature of VO_2), respectively, shown in Figure S17, Supporting Information, and the corresponding photovoltaic parameters are summarized in Table S4, Supporting Information. It can be seen that the V_{oc} of the PSC with VO_2 layer was gradually decreased when elevating from 25 to 65 °C, as well as FF. This is related to the increased intrinsic carrier concentration of perovskite absorber layer which in turn will increase the dark saturation current and thus reduce the V_{oc} and FF. However, it suddenly increased when the temperature reached 85 °C. In this work, there is no difference for the VO_2-based PSC at low temperature (25 °C, 45 °C, 65 °C) and high temperature except for the phase-transition of VO_2. Consequently, the enhanced device performance of VO_2-based PSC at 85 °C was attributed to the phase-transition feature of VO_2 extraction layer. Although the perovskite absorber itself leads to the V_{oc} and FF losses for the device at elevated temperature, it also depends on technological issues linked to carrier transport such as contact resistances.[59] In this work, the faster carrier collection and transportation at the interface of PCBM/BCP and Ag for the VO_2-based device at 85 °C high temperature is of great significance influence on device performance. As mentioned in Figure 1a, the VO_2 at room temperature in VO_2-based PSC is monoclinic VO_2 (M phase), but the VO_2 at high temperature in VO_2-based PSC is rutile VO_2 (R phase). Meanwhile, the electron mobility shown in Figure S18, Supporting Information, for these two phases are quite different from each other. It can be clearly indicated that the electron mobility of VO_2 at 85 °C was nearly 100 times higher than that of VO_2 at room temperature, which can directly suggest the enhanced charge extraction ability at

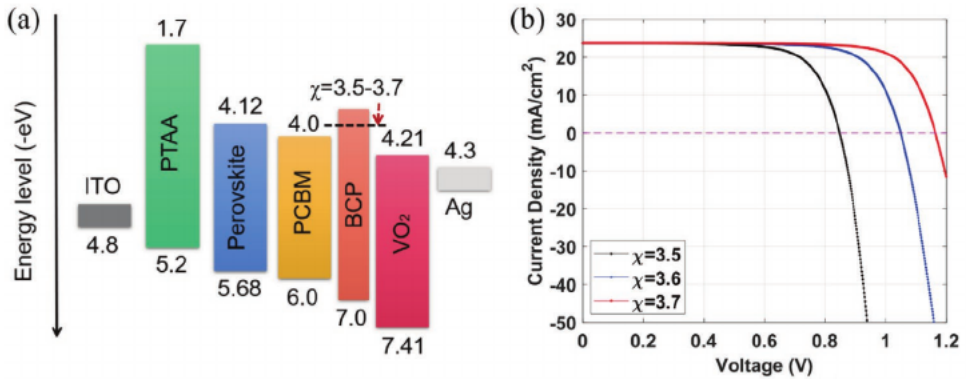

Figure 6. a) The energy diagram of the PSCs with VO_2 layer. b) The corresponding simulated *J–V* curves of the device.

high temperature. According to the theoretical calculation (Figure S19 and Table S5, Supporting Information), it can be qualitatively concluded that VO_2 (R) at 85 °C shows the "metallic" state without the bandgap, while VO_2 (M) at room temperature demonstrates the "insulator" state, indicating the excellent electrical properties of VO_2 (R), which is consistent with Figure 1g and Figure S18, Supporting Information. Also, such a high temperature can increase electron kinetic energy and facilitate the electron tunneling process compared to room temperature, which contributes to the increased J_{sc}.

In order to further understand the potential mechanism behind the improvement of device with VO_2 layer at 85 °C, we want to further indicate the electron affinity or the LUMO level of BCP will affect the device performance with VO_2 layer inserted. To phenomenologically understand the tunneling effect, the drift-diffusion model is used to simulate the changed *J–V* characteristics when the electron affinity of BCP layer is gradually lowered from $\chi = 3.5$ to $\chi = 3.7$ (See **Figure 6** for the band structure in simulation and other simulation parameters and numerical details can be found in our previous works.[60,61]). At the room temperature, the electron affinity of BCP layer is lowered from $\chi = 3.5$ to $\chi = 3.6$ (Figure 6a) due to the inserted VO_2 layer and the corresponding *J–V* curves at room temperature indicated higher V_{oc} and FF (Figure 6b), which is consistent with the experimental *J-V* curves. As shown in Figure S20, Supporting Information, the work function of the VO_2 metallic phase was estimated to be around 4.25 eV, which is lower than that of VO_2 at room temperature. At 85 °C, the VO_2 is phased changed to be the metallic phase with lower work function, leading to the lower electron affinity of BCP, which is further lowered from $\chi = 3.6$ to $\chi = 3.7$. Therefore, the V_{oc} and FF shown in Figure 6b were increased, confirming that the faster charge extraction and transportation at the interface will be dominant to enhance the device performance for VO_2-based PSC at 85 °C. In conclusion, the pronounced increased V_{oc} and FF are correlated with the lowered barrier and pinning of Fermi level caused by the electron tunneling. The electron tunneling in the PCBM/BCP/VO_2 structure should be better than that in the PCBM/BCP/Ag structure, especially when the VO_2 is phased changed to be a metallic phase at high temperature, which will further lower the extraction barrier between the Ag and BCP, considering the enhanced V_{oc} and FF simultaneously and no treatments for the perovskite layer and its contact interfaces.

To verify the feasibility of employing VO_2 in enhancing device stability, a comprehensive study was carried out on both devices under different stress conditions. It can be apparently seen in **Figure 7**a, the perovskite film covered by PCBM/VO_2 (Sample C) shows the better stability compared with bare perovskite film (Sample A), or perovskite film covered by PCBM (Sample B) under all three conditions. Both Figures S21 and S22a, Supporting Information show superior stability of device based on VO_2 layer under ambient conditions. The VO_2-PSC maintained approximately over 90% of its initial PCE after 1000 h, whereas the pristine device without VO_2 layer retained only approximately 30% of its initial PCE after 400 h under relatively high humidity condition. In addition, Figure S22b,c, Supporting Information, show the thermal stability of devices with and without VO_2 layers under 65 and 85 °C without any encapsulation, respectively.

Take Figure S21c, Supporting Information, as an example, the device without VO_2 layer shows poor thermal stability, losing 50% of its initial PCE within 200 h. Comparatively, the device with VO_2 layer retains over 85% under 85 °C. More importantly, long-term operational stability of the encapsulated devices was tested under 1 sun irradiation in an N_2-filled glovebox at an elevated temperature of 85 °C shown in Figure 7b. The device with VO_2 layer could obtain over 90% of its initial value after 1000 h of aging, indicating that it is among the most stable inverted PSCs measured under MPP tracking at 85 °C. From the above discussion, we offer a promising and unique approach for the commercialization of perovskite photovoltaic technology with high efficiency and long-term stability.

3. Conclusions

By employing thermally-induced phase-change material VO_2 as an efficient electron extraction layer in an inverted PSC, we have demonstrated an effective strategy to improve device performance and its operational stability. Benefiting from the suitable cascade band alignment of PCBM/BCP/VO_2, which can effectively reduce the interfacial charge recombination and facilitate the carrier extraction, the champion device has achieved an efficiency of 22.11%, thus outperforming the

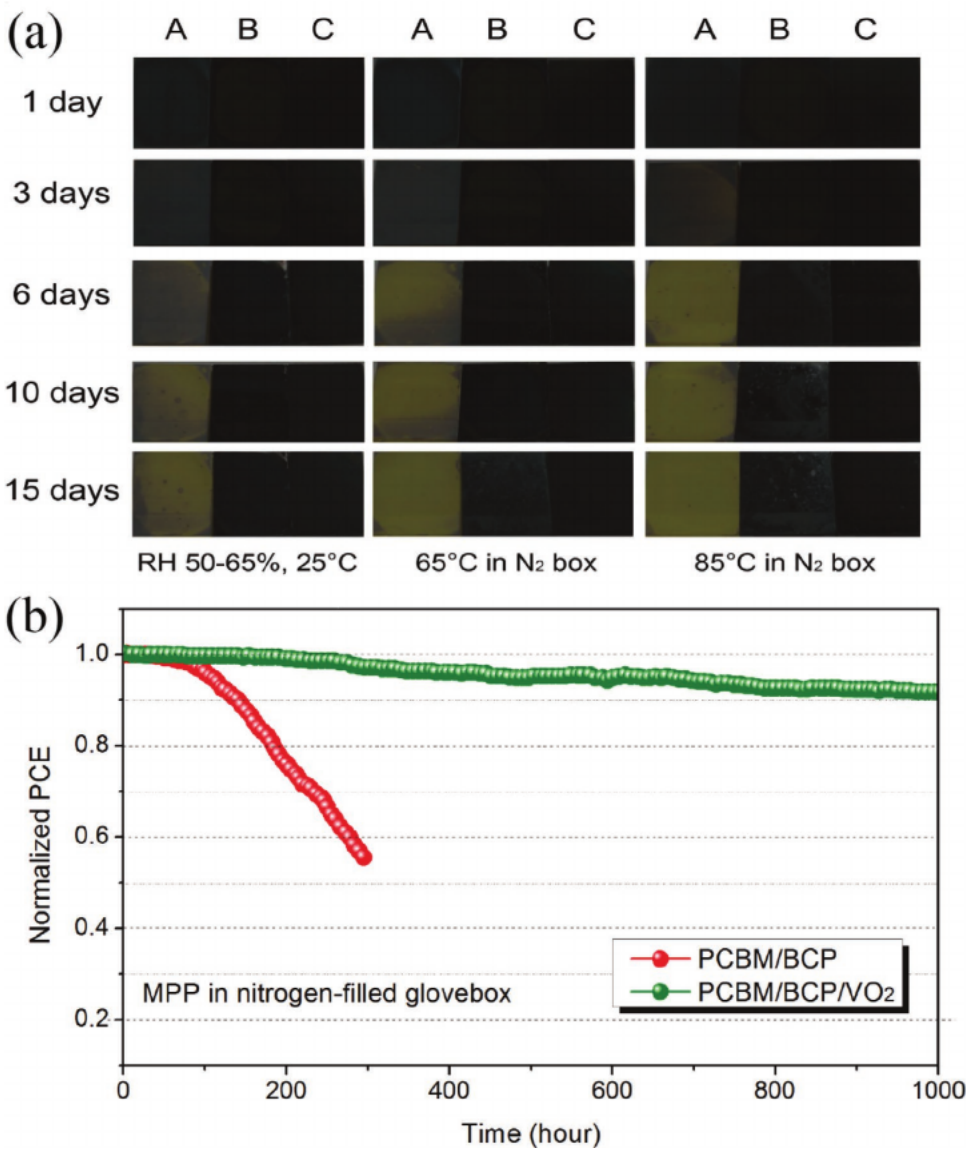

Figure 7. a) Photographs of perovskite film samples coated by different ETLs under various stress conditions. Sample A: bare perovskite film, Sample B: perovskite covered by PCBM, Sample C: perovskite covered by PCBM/VO_2 layers. b) Long-term operational stability of the encapsulated PSCs under MPP tracking at 85 °C under continuous light irradiation with a white LED lamp (100 mW cm^{-2}) in an N_2-filled glovebox.

control device with a lower PCE of 20.96%. More importantly, due to the dramatic change in the electrical properties and better band alignment by phase transition process, the PCE has achieved a steady-state PCE of over 23% at 85 °C. Additionally, it should be noted that the VO_2-based device exhibits outstanding stability under various stress conditions, especially when it is under the 85 °C heat operational condition. To sum up, the outstanding performance of VO_2PSC opens avenue for a new strategy that can simultaneously enhance the efficiency and stability of PSCs with thermally-induced phase-change materials.

Supporting Information

Supporting Information is available from the Wiley Online Library or from the author.

Acknowledgements

X.L. and Y.M. contributed equally to this work. This work was co-financed by National Natural Science Foundation of China (Grant No. 51572098 and 51632006), National Basic Research Program of China (Grant No. 2013CB632500), Natural Science Foundation of Hubei Province (Grant No. 2015CFB432), Open Fund of State Key Laboratory of Advanced Technology (No. 2016-KF-5). In addition, Y.L. acknowledges the National Research Foundation, Prime Minister's Office, Singapore under its Campus for Research Excellence and Technologies Enterprise (CREATE) program and Singapore Ministry of Education (MOE) Academic Research Fund Tier 1 RG103/19 and RG86/20 for funding support. The technical assistance from the Analytical and Testing Center of HUST and NTU is likewise gratefully acknowledged.

Conflict of Interest

The authors declare no conflict of interest.

Data Availability Statement

Research data are not shared.

Keywords

electron extraction layers, high temperature, long-term stability, perovskite solar cells, VO_2 phase-change materials

Received: September 13, 2021
Revised: October 8, 2021
Published online:

[1] M. Grätzel, *Nat. Mater.* **2014**, *13*, 838.
[2] M. A. Green, A. Ho-Baillie, H. J. Snaith, *Nat. Photonics* **2014**, *8*, 506.
[3] W. Zhang, G. E. Eperon, H. J. Snaith, *Nat. Energy* **2016**, *1*, 16048.
[4] J. P. Correa-Baena, A. Abate, M. Saliba, W. Tress, T. J. Jacobsson, M. Grätzel, A. Hagfeldt, *Energy Environ. Sci.* **2017**, *10*, 710.
[5] D. Zhao, C. Chen, C. Wang, M. M. Junda, Z. Song, C. R. Grice, Y. Yu, C. Li, B. Subedi, N. J. Podraza, X. Zhao, G. Feng, R. G. Xiong, K. Zhu, Y. Yan, *Nat. Energy* **2018**, *3*,1093.
[6] X. Li, J. Yang, Q. Jiang, H. Lai, S. Li, J. Xin, W. Chu, J. Hou, *ACS Nano* **2018**, *12*, 5605.
[7] H. Lu, Y. Liu, P. Ahlawat, A. Mishra, W. R. Tress, F. T. Eickemeyer, Y. Yang, F. Fu, Z. Wang, C. E. Avalos, B. I. Carlsen, A. Agarwalla, Z. X, X. Li, Y. Zhan, S. M. Zakeeruddin, L. Emsley, U. Rothlisberger, L. Zheng, A. Hagfeldt, M. Grätzel, *Science* **2020**, *370*, 74.
[8] Y. Jiang, S. C. Yang, Q. Jeangros, S. Pisoni, T. Moser, S. Buecheler, A. N. Tiwari, F. Fu, *Joule* **2020**, *4*, 1087.
[9] A. Kojima, K. Teshima, Y. Shirai, T. Miyasaka, *J. Am. Chem. Soc.* **2009**, *131*, 6050.
[10] J. J. Yoo, G. Seo, M. R. Chua, T. G. Park, Y. Lu, F. Rotermund, Y. K. Kim, C. S. Moon, N. J. Jeon, J. P. Correa-Baena, V. Bulović, S. S. Shin, M. G. Bawendi, J. Seo, *Nature* **2021**, *590*, 587.
[11] K. Xiao, R. Lin, Q. Han, Y. Hou, Z. Qin, H. T. Nguyen, J. Wen, M. Wei, V. Yeddu, M. I. Saidaminov, Y. Gao, L. X. , Y. Wang, H. Gao, C. Zhang, J. Xu, J. Zhu, E. H. Sargent, H. Tan, *Nat. Energy* **2020**, *5*, 870.
[12] Y. Hou, E. Aydin, M. D. Bastiani, C. Xiao, F. H. Isikgor, D. J. Xue, B. Chen, H. Chen, B. Bahrami, A. H. Chowdhury, A. Johnston, S. W. Baek, Z. Huang, M. Wei, Y. Dong, J. Troughton, R. Jalmood, A. J. Mirabelli, T. G. Allen, E. V. Kerschaver, M. I. Saidaminov, D. Baran, Q. Qiao, K. Zhu, S. D. Wolf, E. H. Sargent, *Science* **2020**, *367*, 1135.
[13] A. Al-Ashouri, E. Köhnen, B. Li, A. Magomedov, H. Hempel, P. Caprioglio, J. A. Márquez, A. B. M. Vilches, E. Kasparavicius, J. A. Smith, N. Phung, D. Menzel, M. Grischek, L. Kegelmann, D. Skroblin, C. Gollwitzer, T. Malinauskas, M. Jošt, G. Matič, B. Rech, R. Schlatmann, M. Topič, L. Korte, A. Abate, B. Stannowski, D. Neher, M. Stolterfoht, T. Unold, V. Getautis, S. Albrecht, *Science* **2020**, *370*, 1300.
[14] A. Al-Ashouri, A. Magomedov, M. Roß, M. Jošt, M. Talaikis, G. Chistiakova, T. Bertram, J. A. Márquez, E. Köhnen, E. Kasparavičius, S. Levcenco, L. Gil-Escrig, C. J. Hages, R. Schlatmann, B. Rech, T. Malinauskas, T. Unold, C. A. Kaufmann, L. Korte, G. Niaura, V. Getautis, S. Albrecht, *Energy Environ. Sci.* **2019**, *12*, 3356.
[15] X. Zheng, Y. Hou, C. Bao, J. Yin, F. Yuan, Z. Huang, K. Song, J. Liu, J. Troughton, N. Gasparini, C. Zhou, Y. Lin, D. J. Xue, B. Chen, A. K. Johnston, N. Wei, M. N. Hedhili, M. Wei, A. Y. Alsalloum, P. Maity, B. Turedi, C. Yang, D. Baran, T. D. Anthopoulos, Y. Han, Z. H. Lu, O. F. Mohammed, F. Gao, E. H. Sargent, O. M. Bakr, *Nat. Energy* **2020**, *5*,131.
[16] B. Li, Y. Xiang, K. D. G. I. Jayawardena, D. Luo, Z. Wang, X. Yang, J. F. Watts, S. Hinder, M. T. Sajjad, T. Webb, H. Luo, I. Marko, H. Li, S. A. J. Thomson, R. Zhu, G. Shao, S. J. Sweeney, S. R. P. Silva, W. Zhang, *Nano Energy* **2020**, *78*,105249.
[17] Z. W. Gao, Y. Wang, D. Ouyang, H. Liu, Z. Huang, J. Kim, W. C. H. Choy, *Small Methods* **2020**, *4*, 2000478.
[18] W. Sun, Y. Li, S. Ye, H. Rao, W. Yan, H. Peng, Y. Li, Z. Liu, S. Wang, Z. Chen, X. L, Z. Bian, C. Huang, *Nanoscale* **2016**, *8*, 10806.
[19] H. Zhang, H. Wang, C. C. C. H. Zhu, W. Chen, S. Yang, A. K. Y. Jen, *Adv. Energy Mater.* **2018**, *8*, 1702762.
[20] Y. Chen, Z. Yang, X. Jia, Y. Wu, N. Yuan, J. Ding, W. H. Zhang, S. Liu, *Nano Energy* **2019**, *61*, 148.
[21] L. Xu, Y. Li, C. Zhang, Y. Liu, C. Zheng, W. Lv, M. Li, Y. Chen, W. Huang, R. Chen, *Sol. Energy Mater. Sol. Cells* **2020**, *206*, 110316.
[22] X. Li, J. Yang, Q. Jiang, W. Chu, D. Zhang, Z. Zhou, J. Xin, *ACS Appl. Mater. Interfaces* **2017**, *9*, 41354.
[23] S. Wu, Z. Li, M. Q. Li, Y. Diao, F. Lin, T. Liu, J. Zhang, P. Tieu, W. Gao, F. Qi, X. Pan, Z. Xu, Z. Zhu, A. K. Y. Jen, *Nat. Nanotechnol.* **2020**, *15*, 934.
[24] A. F. Akbulato, L. A. Frolova, M. P. Griffin, I. R. Gearba, A. Dolocan, D. A. V. Bout, S. Tsarev, E. A. Katz, A. F. Shestakov, K. J. Stevenson, P. A. Troshin, *Adv. Energy Mater.* **2017**, *7*, 1700476.
[25] J. Lian, B. Lu, F. Niu, P. Zeng, X. Zhan, *Small Methods* **2018**, *2*, 1800082.
[26] L. Meng, J. You, T. F. Guo, Y. Yang, *Acc. Chem. Res.* **2016**, *49*, 155.
[27] M. S. Selim, A. M. Elseman, Z. Hao, *ACS Appl. Energy Mater.* **2020**, *3*, 11781.
[28] S. Wu, R. Chen, S. Zhang, B. H. Babu, Y. Yue, H. Zhu, Z. Yang, C. Chen, W. Chen, Y. Huang, S. Fang, T. Liu, L. Han, W. Chen, *Nat. Commun.* **2019**, *10*, 1161.
[29] Z. Zhu, Y. Bai Y, X. Liu, C. C. Chueh, S. Yang, A. K. Y. Jen, *Adv. Mater.* **2016**, *28*, 6478.
[30] X. Hu, C. Liu, Z. Zhang, X. F. Jiang, J. Garcia, C. Sheehan, L. Shui, S. Priya, G. Zhou, S. Zhang, K. Wang, *Adv. Sci.* **2020**, *7*, 2001285.
[31] Y. Ke, Y. Yin, Q. Zhang, Y. Tan, P. Hu, S. Wang, Y. Tang, Y. Zhou, X. Wen, S. Wu, T. J. White, J. Yin, J. Peng, Q. Xiong, D. Zhao, Y. Long, *Joule* **2019**, *3*, 858.
[32] M. Vaseem, S. Zhen, S. Yang, W. Li, A. Shamim, *Adv. Electron. Mater.* **2019**, *5*, 1800949.
[33] H. Ji, D. Liu, C. Zhang, H. Cheng, *Sol. Energy Mater. Sol. Cells* **2018**, *176*, 1.
[34] T. D. Vu, S. Liu, X. Zeng, C. Li, Y. Long, *Ceram. Int.* **2020**, *46*, 8145.
[35] Y. Ke, Q. Zhang, T. Wang, S. Wang, N. Li, G. Lin, X. Liu, Z. Dai, J. Yan, J. Yin, S. Magdassi, D. Zhao, Y. Long, *Nano Energy* **2020**, *73*, 104785.
[36] J. M. Gonçalves, M. I. da Silva, L. Angnes, K. Araki, *J. Mater. Chem. A* **2020**, *8*, 2171.
[37] S. S. Majid, S. R. Sahu, A. Ahad, K. Dey, K. Gautam, F. Rahman, P. Behera, U. Deshpande, V. G. Sathe, D. K. Shukla, *Phys. Rev. B* **2020**, *101*, 014108.
[38] K. A. Bush, C. D. Bailie, Y. Chen, A. R. Bowring, W. Wang, W. Ma, T. Leijtens, F. Moghadam, M. D. McGehee, *Adv. Mater.* **2016**, *28*, 3937.
[39] X. Jia, L. Zhang, Q. Luo, H. Lu, X. Li, Z. Xie, Y. Yang, Y. Q. Li, X. Liu, C. Q. Ma, *ACS Appl. Mater. Interfaces* **2016**, *8*, 18410.
[40] P. Ru, E. Bi, Y. Zhang, Y. Wang, W. Kong, Y. Sha, W. Tang, P. Zhang, Y. Wu, W. Chen, X. Yang, H. Chen, L. Han, *Adv. Energy Mater.* **2020**, *10*, 1903487.
[41] S. Yang, J. Dai, Z. Yu, Y. Shao, Y. Zhou, X. Xiao, X. C. Zeng, J. Huang, *J. Am. Chem. Soc.* **2019**, *141*, 5781.
[42] X. Li, J. Yang, Q. Jiang, H. Lai, S. Li, Y. Tan, Y. Chen, S. Li, *J. Mater. Chem. A* **2019**, *7*, 7065.

[43] Y. Li, Y. Zhao, Q. Chen, Y. Yang, Y. Liu, Z. Hong, Z. Liu, Y. T. Hsieh, L. Meng, Y. Li, Y. Yang, *J. Am. Chem. Soc.* **2015**, *137*, 15540.
[44] T. M. Clarke, C. Lungenschmied, J. Peet, N. Drolet, A. J. Mozer, *Adv. Energy Mater.* **2015**, *5*, 1401345.
[45] L. Wan, W. Zhang, S. Fu, L. Chen, Y. Wang, Z. Xue, Y. Tao, W. Zhang, W. Song, J. Fang, *J. Mater. Chem. A* **2020**, *8*, 6517.
[46] Q. Jiang, Y. Zhao, X. Zhang, X. Yang, Y. Chen, Z. Chu, Q. Ye, X. Li, Z. Yin, J. You, *Nat. Photonics* **2019**, *13*, 460.
[47] Y. Liu, Y. Chen, *Adv. Mater.* **2020**, *32*, 1805843.
[48] W. Chen, K. Li, Y. Wang, X. Feng, Z. Liao, Q. Su, X. Lin, Z. He, *J. Phys. Chem. Lett.* **2017**, *8*, 591.
[49] P. N. Murgatroyd, *J. Phys. D: Appl. Phys.* **1970**, *3*, 151.
[50] M. Samiee, S. Konduri, B. Ganapathy, R. Kottokkaran, H. A. Abbas, A. Kitahara, P. Joshi, L. Zhang, M. Noack, V. Dalal, *Appl. Phys. Lett.* **2014**, *105*, 153502.
[51] S. Zhang, Z. Liu, W. Zhang, Z. Jiang, W. Chen, R. Chen, Y. Huang, Z. Yang, Y. Zhang, L. Han, W. Chen, *Adv. Energy Mater.* **2020**, *10*, 2001610.
[52] C. Chen, S. Zhang, S. Wu, W. Zhang, H. Zhu, Z. Xiong, Y. Zhang, W. Chen, *RSC Adv.* **2017**, *7*, 35819.
[53] Z. Ying, X. Yang, J. Zheng, Y. Zhu, J. Xiu, W. Chen, C. Shou, J. Sheng, Y. Zeng, B. Yan, H. Pan, J. Ye, Z. He, *J. Mater. Chem. A* **2021**, *9*, 12009.
[54] H. S. Kim, I. Mora-Sero, V. Gonzalez-Pedro, F. Fabregat-Santiago, E. J. Juarez-Perez, N. G. Park, J. Bisquert, *Nat. Commun.* **2013**, *4*, 2242.
[55] K. Yan, Z. Wei, J. Li, H. Chen, Y. Yi, X. Zheng, X. Long, Z. Wang, J. Wang, J. Xu, S. Yang, *Small* **2015**, *11*, 2269.
[56] B. Wu, K. Fu, N. Yantara, G. Xing, S. Sun, T. C. Sum, N. Mathews, *Adv. Energy Mater.* **2015**, *5*, 1500829.
[57] X. Ren, Z. S. Wang, W. C. H. Choy, *Adv. Opt. Mater.* **2019**, *7*, 1900407.
[58] T. Moot, J. B. Patel, G. McAndrews, E. J. Wolf, D. Morales, I. E. Gould, B. A. Rosales, C. C. Boyd, L. M. Wheeler, P. A. Parilla, S. W. Johnston, L. T. Schelhas, M. D. McGehee, J. M. Luther, *ACS Energy Lett.* **2021**, *6*, 2038.
[59] O. Dupré, R. Vaillon, M. A. Green, *Sol. Energy Mater. Sol. Cells* **2015**, *140*, 92.
[60] X. Ren, Z. Wang, W. E. I. Sha, W. C. H. Choy, *ACS Photonics* **2017**, *4*, 934.
[61] Z. S. Wang, W. E. I. Sha, W. C. H. Choy, *J. Appl. Phys.* **2016**, *120*, 213101.